



## Available online at www.sciencedirect.com

## **ScienceDirect**

Comput. Methods Appl. Mech. Engrg. 387 (2021) 114166

Computer methods in applied mechanics and engineering

www.elsevier.com/locate/cma

# Stochastic Modeling and identification of material parameters on structures produced by additive manufacturing

Shanshan Chu<sup>a</sup>, Johann Guilleminot<sup>a</sup>,\*, Cambre Kelly<sup>b</sup>, Bijan Abar<sup>b</sup>, Ken Gall<sup>b</sup>

<sup>a</sup> Department of Civil and Environmental Engineering, Duke University, Durham, NC 27708, USA
<sup>b</sup> Department of Mechanical Engineering and Materials Science, Duke University, Durham, NC 27708, USA

Received 25 June 2021; received in revised form 27 August 2021; accepted 29 August 2021 Available online xxxx

#### **Abstract**

A methodology enabling the representation, sampling, and identification of spatially-dependent stochastic material parameters on complex structures produced by additive manufacturing is presented. The modeling component builds upon earlier works by the authors and relies on the combination of two ingredients. First, a fractional stochastic partial differential equation is introduced and parameterized in order to automatically capture the complex features of additively manufactured parts. Information-theoretic transport maps are subsequently introduced with the aim of ensuring well-posedness in the forward propagation problem. The identification of stochastic elasticity tensors on titanium scaffolds produced by laser powder bed fusion is then discussed. To this end, we consider an isotropic approximation at a mesoscale where fluctuations are aggregated over several layers, and address both the calibration and validation of the probabilistic model by using different sets of physical structural experiments. Despite the high sensitivity of the forward map to applied boundary conditions, geometrical parameters, and structural porosity, it is shown that the calibrated stochastic model can generate non-vanishing probability levels for all experimental observations.

© 2021 Elsevier B.V. All rights reserved.

Keywords: Additive manufacturing; Complex geometry; Random field; Stochastic modeling; Uncertainty quantification

## 1. Introduction

By enabling the processing of parts with unprecedented levels of complexity over multiple length scales, additive manufacturing (AM) has opened new realms in terms of on-demand manufacturing for a wide class of engineered and biological materials. While disruptive, AM technologies also raise formidable challenges with regard to material characterization, simulations for design and optimization, and certification and qualification. Of particular interest in this work are the geometrical and material uncertainties that are often exhibited by 3D printed materials and structures [1]. In this context, uncertainty quantification (UQ) techniques have been deployed over the past decade with the goal of managing, predicting, and ultimately reducing (part of) these uncertainties [1,2]. Most of the results reported so far have primarily focused on the modeling and propagation of uncertainties in AM processes. The influence of manufacturing parameters, such as laser power, scan length, and scanning speed, was investigated

E-mail address: johann.guilleminot@duke.edu (J. Guilleminot).

<sup>\*</sup> Corresponding author.

in, e.g., [2–6] (see [7] for a review on metal laser powder bed fusion manufacturing for instance). UQ analyses integrating multiphysics aspects during, e.g., the melting and solidification stages, were specifically proposed in [8–13]. Given the high computational cost associated with the forward propagation of uncertainties through additive manufacturing models, surrogate representations are often adopted; see [14] for the use of Kriging to efficiently propagate uncertainties from process parameters to microstructural data, and from the fine-scale description to the structural response for example (see also [15] for UQ-informed multiscale constitutive models for polycrystalline materials).

In this work, we consider the construction and identification of suitable probabilistic representations for material parameters on final AM parts, with the aim of enabling the integration of aleatoric material uncertainties in subsequent computational analyses. These models can be used as prior surrogates in the identification and propagation of stochastic constitutive models, and may be calibrated by using either UO-based simulations for AM technologies (as described above), or physical experiments on as-built structures (see [16] for a calibration methodology at mesoscale using digital image correlation). The development of such representations is challenging due to a number of factors. First, the statistical variations that are typically observed at a given scale are often spatially varying, meaning that material parameters of interest must be modeled as random fields. In practice, most fundamental properties of these fields, such as the level of anisotropy and the underlying covariance structures, are strongly influenced by manufacturing conditions (which generate process-specific space-time memory), as well as by the geometrical complexity of the structure to be produced. Capturing these features remains a daunting task from a stochastic modeling standpoint. Second, most UQ frameworks involve Karhunen-Loève expansions for random fields [17], which require covariance functions to be defined a priori. While standard (e.g., exponential) covariance models can readily be used on curved domains through proper parameterization [18], their application to nonisotropic covariance structures—which are expected in AM products—is hardly tractable. Third, model parameters must usually be identified based on limited amounts of data, which highlights the need to construct stochastic models with low-dimensional hyperparameters.

Motivated by these problems, we propose a stochastic modeling framework for random fields of material parameters on structures produced by additive manufacturing. Following earlier contributions by the authors [19–21], the methodology builds on the combination of a fractional stochastic partial differential equation, which is specifically defined in this work to capture the complex features of the additively manufactured geometry, and information-theoretic measure transports, which are introduced to obtain least-informative models ensuring well-posedness in the forward propagation problem. While the framework can be applied to any material properties—at the expense of adapting the transport maps primarily—, we consider the modeling of elasticity fields for the sake of illustration and discuss the choice of a suitable, process-inferred parameterization. We also address the identification of the proposed model using a set of physical (structural) experiments, and discuss some validation aspects.

The rest of this paper is organized as follows. In Section 2, we present the mathematical formulation for the stochastic model of material uncertainties. Section 3 is devoted to the identification and validation of the proposed approach, using physical experiments. Concluding remarks are finally provided in Section 4.

## 2. Description of the probabilistic modeling framework

In this section, we propose a stochastic modeling approach for spatially-varying material parameters on geometries processed by additive manufacturing. Without loss of generality, we consider the case of laser powder bed fusion (LPBF) and the prototypical geometry shown in Fig. 1 for illustration purposes. This geometry is a titanium scaffold with a gyroid-sheet microarchitecture that is typically used in bone tissue engineering (see Section 3.1 for further details). It will be used throughout this section to exemplify key features of the methodology and to provide numerical examples.

Depending on the ultimate goal of the simulations, the fields of material parameters can be described at various scales, ranging from the microscopic scale (which is the scale of the polycrystalline microstructure where grain-resolved mechanical fields are considered) to any mesoscopic scales where properties exhibit smoother spatial fluctuations. Fracture simulations, for instance, may be instantiated at the mesoscale corresponding to depository layers where local defects, such as porosities, critically contribute to localization and damage initiation. On the other hand, a bulk elastic response used for, e.g., design optimization, may be evaluated at a coarser resolution—typically that of a few layers. The choice of the modeling scale is therefore application-dependent and has important consequences on the functional forms retained in the probabilistic model, on the parameterization of the latter, as well as on the computational cost associated with numerical experiments. These aspects will be explored in the following sections.

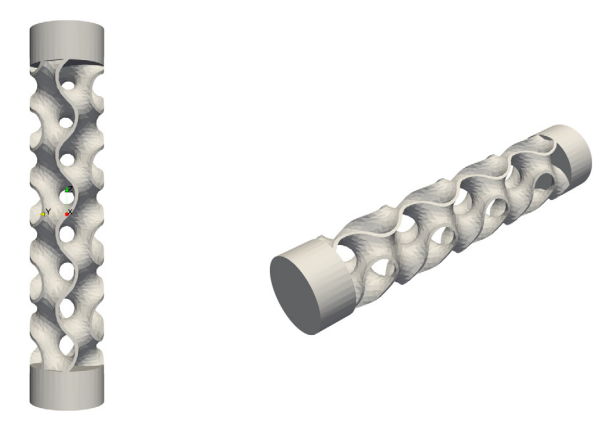


Fig. 1. Stereolithographic representation of the 3D printed geometry.

## 2.1. Stochastic modeling approach

Let  $\Omega \subset \mathbb{R}^3$  be the connected, open domain (with boundary  $\partial \Omega$ ) corresponding to the geometry under consideration. We consider the construction of a probabilistic model for spatially-dependent stochastic material parameters, such as elasticity fields or fields of plasticity parameters. Let  $\{P(x), x \in \Omega\}$  be the second-order multivariate random field of interest, defined on a probability space  $(\Theta, \mathcal{F}, \mathcal{P})$  and with values in a given subset  $S \subseteq \mathbb{R}^n$ . Unless an algebraic preconditioning (through an exponential map, for instance) is used to relax inequality constraints on material parameters, the set S is generally bounded or semi-bounded. We therefore assume that  $S \subset \mathbb{R}^n$  from now on and as a result, the random field  $\{P(x), x \in \Omega\}$  is non-Gaussian. With a view towards an identification based on limited physical experiments, we seek a low-dimensional surrogate representation in the form

$$P(x) = \mathcal{T}(\Xi(x), x) , \quad \forall x \in \Omega , \tag{1}$$

where  $\{\mathcal{T}(\cdot,x)\}_{x\in\Omega}$  is a family of transport maps and  $\{\Xi(x),x\in\mathbb{R}^3\}$  is a normalized Gaussian random field with statistically independent components in  $\mathbb{R}^n$ ,  $\mathbb{E}\{\Xi_i(x)\Xi_j(x)\}=\delta_{ij}$ . Holding x fixed in  $\Omega$ ,  $\mathcal{T}(\cdot,x)$  pushes forward the standard normal vector  $\Xi(x)\sim\mathcal{N}(\mathbf{0}_n,[I_n])$  into the non-Gaussian random vector  $P(x)\sim\pi_x$ , where  $\mathbf{0}_n$  is the null vector of length n,  $[I_n]$  is the  $n\times n$  identity matrix, and  $\pi_x$  denotes a target probability law. The definition of the family  $\{\pi_x\}_{x\in\Omega}$  allows for the modeling of nonhomogeneous random fields and enables the prescription of the family of first-order marginal probability distributions for the random field  $\{P(x),x\in\Omega\}$ . It should be noticed that the action of the transport maps on the underlying Gaussian field  $\{\Xi(x),x\in\mathbb{R}^3\}$ , together with the correlation function of the latter, defines the complete system of marginal distributions of  $\{P(x),x\in\Omega\}$ .

The identification of random fields exhibiting a nonhomogeneous first-order marginal distribution, while theoretically feasible, is generally limited by the availability of relevant experimental information (or lack thereof). For this reason, we consider the case of a spatially-independent transport map, writing  $P(x) = \mathcal{T}(\Xi(x))$  for all x in  $\Omega$ , and accordingly denote by  $\pi$  the target probability distribution. The stochastic modeling approach then involves two ingredients. The first aspect pertains to the definition of the underlying Gaussian random field  $\{\Xi(x), x \in \mathbb{R}^3\}$  on nonconvex domains such as the one shown in Fig. 1. One major challenge here is to define the field in such a way that its covariance function captures both the layered structure induced by the AM process and the complex architecture of the geometry. The second component is concerned with the construction of the target probability law  $\pi$ . These two ingredients are reviewed in Sections 2.2 and 2.3, respectively.

## 2.2. Definition of the underlying Gaussian field on AM geometries

Let us first recall that  $\{\Xi_i(x), x \in \mathbb{R}^3\}$  and  $\{\Xi_j(x), x \in \mathbb{R}^3\}$  are statistically independent Gaussian random fields for  $i \neq j$  by construction. In this work, we model each component of  $\{\Xi(x), x \in \mathbb{R}^3\}$  as a Matérn field. An

isotropic, centered stationary Gaussian random field  $\{\Xi_i(x), x \in \mathbb{R}^3\}$  is said to be of Matérn type if its covariance function reads

$$C(\boldsymbol{x}, \boldsymbol{y}) = \sigma^2 \frac{2^{1-\nu}}{\Gamma(\nu)} \left(\kappa \|\boldsymbol{x} - \boldsymbol{y}\|\right)^{\nu} K_{\nu} \left(\kappa \|\boldsymbol{x} - \boldsymbol{y}\|\right) , \quad \forall \boldsymbol{x}, \boldsymbol{y} \in \mathbb{R}^3 ,$$
 (2)

where  $C(x, y) = \mathbb{E}(\Xi_i(x)\Xi_i(y))$ , with  $\mathbb{E}$  the operator of mathematical expectation. In Eq. (2),  $||x|| = \langle x, x \rangle^{1/2}$  denotes the Euclidean norm of  $x \in \mathbb{R}^3$ , with  $\langle \cdot, \cdot \rangle$  the Euclidean inner product,  $\sigma^2$  is the marginal variance of the field,  $\Gamma$  is the Gamma function,  $\kappa > 0$  and  $\nu > 0$  are the scale and smoothness parameters, and  $K_{\nu}$  is the modified Bessel function of the second kind (of order  $\nu$ ). A Matérn random field is  $\lfloor \nu - 1 \rfloor$  mean-square differentiable and the widely-used exponential and squared exponential covariance functions are obtained for  $\nu = 1/2$  and  $\nu \to +\infty$ , respectively.

According to Whittle [22,23] (see Section 9 in [22]), a Matérn random field can equivalently be defined as the stationary solution to the fractional stochastic partial differential equation (SPDE)

$$\left(\kappa^2 \mathcal{I} - \langle \nabla, \nabla \rangle\right)^{\alpha/2} \Xi_i(x) = \dot{\mathcal{W}}(x) , \quad x \in \mathbb{R}^3 , \tag{3}$$

where  $\mathcal{I}$  and  $\nabla$  are the identity and the gradient operators, respectively,  $\alpha$  is a parameter controlling the smoothness of the solution with  $\alpha = \nu + d/2$  (notice that selecting  $\alpha = 2$  renders the operator in Eq. (3) non-fractional), and  $\{\dot{\mathcal{W}}(x), x \in \Omega\}$  is the spatial normalized Gaussian white noise. The above interpretation recently regained popularity following the work by Lindgren and coworkers, who provided an efficient formulation to solve the fractional SPDE, supplemented with Neumann boundary conditions, on bounded domains [24]. Many applications were proposed since then, ranging from Bayesian inference [25–30] to climate modeling [31] to modeling and optimization in computational mechanics [19–21,32,33]. Extensions involving other types of boundary conditions can be found in [25,34,35], while theoretical generalizations were proposed in [31,36–38]. In particular, the case of anisotropic, nonstationary fields was addressed in [36]. Specifically, the SPDE was modified as

$$\left(\kappa^2 \mathcal{I} - \langle \nabla, [D(\mathbf{x})] \nabla \rangle\right)^{\alpha/2} \Xi_i(\mathbf{x}) = \dot{\mathcal{W}}(\mathbf{x}) , \quad \mathbf{x} \in \Omega , \tag{4}$$

where  $x \mapsto [D(x)]$  is termed the diffusion field (owing to the formal analogy between the SPDE and the heat equation) and takes values in the set of symmetric positive definite matrices. The advantage of defining the random field  $\{\Xi_i(x), x \in \mathbb{R}^3\}$  through Eq. (4) lies in the fact that constructing a proper diffusion field [D] is generally much simpler than defining a nonstationary covariance kernel on complex geometries a priori. In the particular case of AM geometries, the definition of  $x \mapsto [D(x)]$  may partly be inferred from laser trajectory, hence providing a path for the robust integration of manufacturing parameters in the uncertainty quantification framework. Such a construction is presented in Section 2.2.1.

## 2.2.1. Definition of the diffusion field

In order to define the diffusion field  $x \mapsto [D(x)]$  and capture the nonstationary effects that are often experimentally observed in materials produced by AM, we first introduce the decomposition

$$[D(\mathbf{x})] = \sum_{i=1}^{3} \lambda_i \, \phi^i(\mathbf{x}) \otimes \phi^i(\mathbf{x}) \,, \quad \forall \, \mathbf{x} \in \Omega \,\,, \tag{5}$$

where  $\{\lambda_i\}_{i=1}^3$  are strictly positive model parameters defining correlation ranges and  $\{\phi^i\}_{i=1}^3$  are linearly-independent orientation fields controlling the anisotropy of the covariance function. The expansion in Eq. (5) is low-dimensional and presents the additional benefit of being easily interpretable from a physical standpoint when  $\|[D(x)] - [I_3]\| \ll 1$  at point x, with  $[I_3]$  the  $3 \times 3$  identity matrix. In this case, the parameter  $\lambda_i$  specifically controls the correlation range along  $\phi^i(x)$  at that specific location. In order to construct the orientation fields, we assume below that the material is deposited in the  $(e^1, e^2)$  plane, where  $(e^1, e^2, e^3)$  is the canonical basis of  $\mathbb{R}^3$  (the generalization to other situations being straightforward). We then split the construction task into two steps, by considering the definition of  $x \mapsto \phi^1(x)$  and  $x \mapsto \phi^2(x)$  in the horizontal  $(e^1, e^2)$  plane first, and by subsequently addressing the construction of  $x \mapsto \phi^3(x)$ .

In this work, we adopt a mesoscopic representation viewpoint. Specifically, we consider the case where fields are described at, or beyond, the scale of quasi-isotropization, defined by a characteristic length scale denoted by  $\ell$ . In the case of laser powder bed fusion, the laser beam direction is typically rotated by an angle  $\alpha$  (expressed in

degrees) from one layer to the next (in the results presented in Section 3,  $\alpha = 60$  [deg]). Here, the length  $\ell$  is taken such that  $\ell \gtrsim K \times t$ , where t is the thickness of one single layer and K is the smallest, non-zero integer such that  $K \times \alpha \equiv 0 \pmod{360}$  (assuming that  $360 \equiv 0 \pmod{\alpha}$ ). In other words, the length  $\ell$  is set such that the laser beam direction gets back to a previous path angular-wise after (K-1) layers were deposited. This ensures, in particular, that the mesoscopic response of the material is nearly isotropic, even if localized process-induced anisotropy may exist at smaller scales. When material processing is performed along straight paths, regardless of the topology in the  $(e^1, e^2)$  plane, the in-plane orientation fields are defined as

$$\phi^{i}(\mathbf{x}) = \mathbf{e}^{i} , \quad \forall \ \mathbf{x} \in \Omega , \quad i \in \{1, 2\} , \tag{6}$$

owing to the definition of the mesoscopic scale.

The definition of the orientation field  $\phi^3$  turns out to be more challenging as the induced correlation structure must capture topological changes along the vertical direction. In order to tackle this problem, we introduce the fictitious Laplace problem

$$\Delta \Psi(\mathbf{x}) = 0 \ , \quad \forall \ \mathbf{x} \in \Omega \ , \tag{7}$$

supplemented with the Dirichlet boundary conditions

$$\begin{cases} \Psi(\mathbf{x}) = 0 , & \forall \mathbf{x} \in \partial \Omega_b \\ \Psi(\mathbf{x}) = 1 , & \forall \mathbf{x} \in \partial \Omega_t \end{cases}$$
(8)

where  $\partial \Omega_b$  and  $\partial \Omega_t$  are the bottom and top boundaries of the geometry, and with the Neumann boundary condition

$$\langle \nabla \Psi(\mathbf{x}), \mathbf{n}(\mathbf{x}) \rangle = 0 , \quad \forall \mathbf{x} \in \partial \Omega \setminus (\partial \Omega_b \cup \partial \Omega_t) ,$$
 (9)

where n(x) is the outward normal unit vector at location x on the boundary. We subsequently defined the orientation field as

$$\phi^{3}(\mathbf{x}) = \frac{1}{\|\nabla \Psi(\mathbf{x})\|} \nabla \Psi(\mathbf{x}) , \quad \forall \mathbf{x} \in \Omega .$$
(10)

The rationale behind introducing the above potential flow problem is that the velocity vector  $\nabla \Psi$  naturally captures complex boundaries and topological singularities, such as holes, on the fly, hence providing a path towards an algorithmic integration of geometrical features in the parameterization of the diffusion field. The solution of the Laplace equation is obtained by the finite element method with a  $\mathbb{P}_1$  tetrahedral mesh, composed of 53,631 nodes and 208,185 elements (the characteristic element size is h = 0.18 [mm]), and is shown in Fig. 2. Finally, the vector-valued orientation field  $x \mapsto \phi^3(x)$  corresponding to this solution is displayed in Fig. 3.

**Remark 1.** The above construction can easily be extended to address other situations where in-plane laser trajectory accounts for the local topology, or when simulations are performed at the scale of single layers. In the former case, one can consider additional Laplace problems with updated Dirichlet boundary conditions constraining the flow along desired directions, and project the gradients of the solutions thus obtained onto the horizontal plane to define  $\phi^1$  and  $\phi^2$ . In the later case, laser path can directly be plugged into the formulation to define the in-plane directional fields.

## 2.2.2. Sampling scheme

Samples of the statistically independent components of the underlying Gaussian field  $\{\Xi(x), x \in \Omega\}$  can be obtained by solving the SPDE given by Eq. (4) with the parameterization of the diffusion constructed in Section 2.2.1. To this end, we follow the approach proposed in [24] and introduce the finite-dimensional representation

$$\Xi_j(\mathbf{x}) = \sum_{i=1}^N \Xi_i^{(j)} \psi_i(\mathbf{x}) , \qquad (11)$$

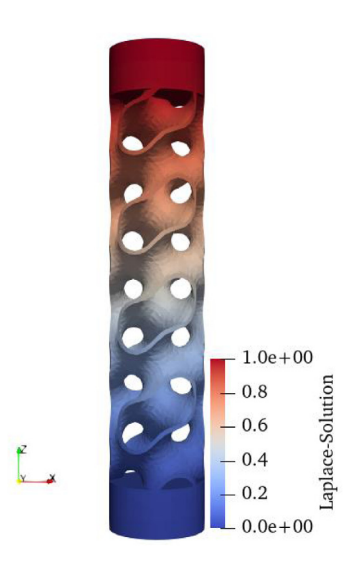


**Fig. 2.** Plot of the solution  $x \mapsto \Psi(x)$  to the Laplace problem defined by Eqs. (7)–(9).



Fig. 3. Plot of the orientation field  $x \mapsto \phi^3(x)$ , defined by Eq. (10), on the bottom part of the geometry.

where  $\{\psi_i\}_{i=1}^N$  is a set of piecewise linear basis functions defined on the finite element mesh (with N nodes), and  $\boldsymbol{\Xi}^{(j)} = (\Xi_1^{(j)}, \dots, \Xi_N^{(j)})^\mathsf{T}$  is the Gaussian random vector of nodal values. For  $\alpha = 2$ , it was shown that the weak Galerkin stochastic solution satisfies

$$\boldsymbol{\mathcal{\Xi}}^{(j)} \sim \mathcal{N}(\mathbf{0}_N, [\Sigma])$$
, (12)

where  ${\mathcal N}$  denotes the normal distribution and the covariance matrix  ${\mathcal \Sigma}$  reads as

$$[\Sigma] = (\kappa^2[M] + [G])^{-1} [M] (\kappa^2[M] + [G])^{-1} , \qquad (13)$$

where the  $(N \times N)$  matrices [M] and [G] have entries defined as

$$M_{ij} = \int_{\mathcal{O}} \psi_i(\mathbf{x}) \psi_j(\mathbf{x}) \, d\mathbf{x} \tag{14}$$

and

$$G_{ij} = \int_{\Omega} \langle \nabla \psi_i(\mathbf{x}), [D(\mathbf{x})] \nabla \psi_j(\mathbf{x}) \rangle d\mathbf{x}$$
(15)

for  $1 \le i, j \le N$ , respectively. From a computational standpoint, it is convenient to alternatively work with the precision matrix

$$[\Sigma]^{-1} = (\kappa^2[M] + [G])[M]^{-1}(\kappa^2[M] + [G]), \qquad (16)$$

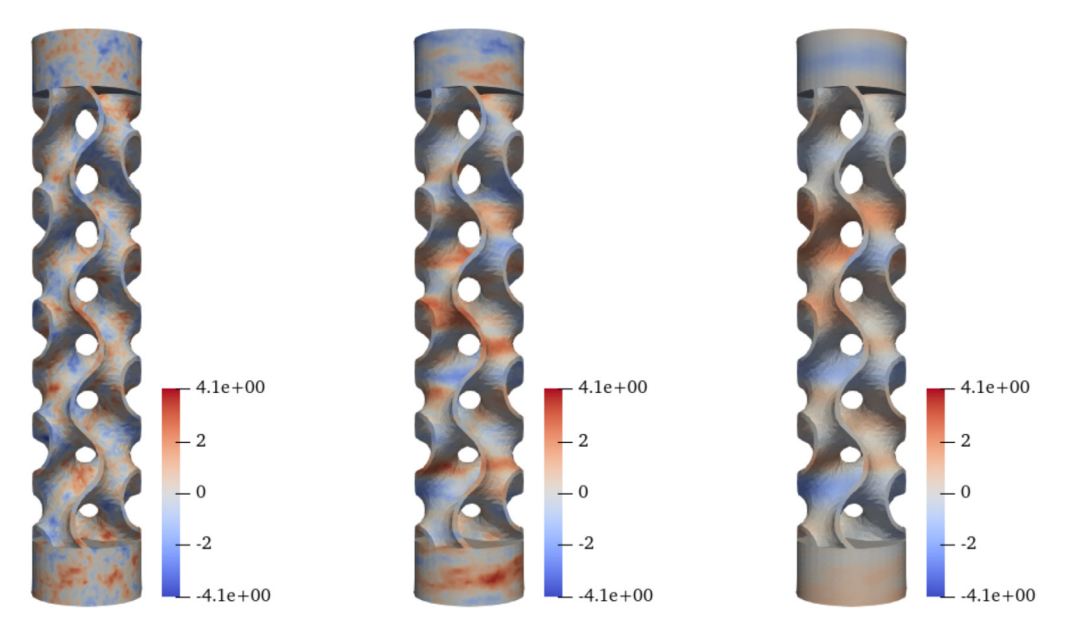


Fig. 4. Plot of realization of the Gaussian random field  $\{\Xi(x), x \in \Omega\}$  for  $\lambda = (\kappa^4/256, \kappa^4/256, \kappa^4/256)$  (quasi-isotropic kernel; left panel),  $\lambda = (\kappa^4/64, \kappa^4/64, \kappa^4/256)$  (moderately anisotropic kernel; middle panel), and  $\lambda = (\kappa^4/16, \kappa^4/16, \kappa^4/256)$  (strongly anisotropic kernel; right panel), with  $\kappa = 6$  [mm].

applying a lumping procedure to evaluate the inverse of the mass matrix [M] efficiently. In this case, a sample  $\boldsymbol{\xi}^{(j)}(\theta)$  of  $\boldsymbol{\Xi}^{(j)}$ ,  $\theta \in \Theta$ , can be obtained by solving the linear system  $[L]\boldsymbol{\xi}^{(j)}(\theta) = \boldsymbol{w}(\theta)$ , where [L] is either the square root or the upper triangular matrix arising in the Cholesky factorization of the precision matrix  $[\Sigma]^{-1}$ , and  $\boldsymbol{w}(\theta)$  denotes a sample of  $\boldsymbol{W} \sim \mathcal{N}(\boldsymbol{0}_N, [I_N])$ . In the former case, a Krylov subspace method can be deployed to generate the samples; see, e.g., [39]. This approach is particularly well suited to handle dense meshes (as it scales as  $\mathcal{O}(N^2)$ , compared to the typical  $\mathcal{O}(N^3)$  scaling for Cholesky factorization), as well as poorly conditioned systems. In the results shown below, the Cholesky factorization method is used to produce independent samples of the stochastic fields.

## 2.2.3. Numerical examples

One sample of a given component of the random field  $\{\Xi(x), x \in \Omega\}$  is shown in Fig. 4 for a quasi-isotropic, a moderately anisotropic, and a strongly anisotropic parameterization of the diffusion field (from the left panel to the right). Here, we take  $\kappa = 6$  [mm], which corresponds to the diameter of the cylindrical top and bottom parts. Notice that in these subpanels, we use the same sample  $w(\theta)$  to ensure meaningful qualitative comparison as the hyperparameter  $\lambda$  changes (see Eq. (5)). As expected, it is seen that setting the in-plane parameters  $\lambda_1$  and  $\lambda_2$  greater than the out-of-plane hyperparameter  $\lambda_3$  leads to an anisotropic stratified structure for the random field realization, owing to the particular definition of the diffusion term [D]. This modeling capability turns out to be specifically well adapted to model stochastic fields generated by additive manufacturing technologies that involve in-plane transient processing conditions (which generate spatial memory, first during in-plane depository, and second through depository on the adjacent layers). This key observation can also be made on the correlation structure for the field, which is here estimated with respect to an arbitrary point in the mid-plane of the geometry; see Fig. 5. Specifically, retaining larger values for  $\lambda_1$  and  $\lambda_2$  induces a larger correlation range within the horizontal plane, which is consistent with the qualitative assessment made on the realizations. It is also observed that the formulation naturally captures the structure of the underlying geometry on the fly: in particular, points located nearby with respect to the standard Euclidean distance can properly have small to zero cross-correlation coefficients depending on the local topology. It should be noticed that reproducing such a behavior without the proposed parameterization is extremely difficult, as the covariance kernel turns out to be nonstationary—and hence, hard to define in closed form.

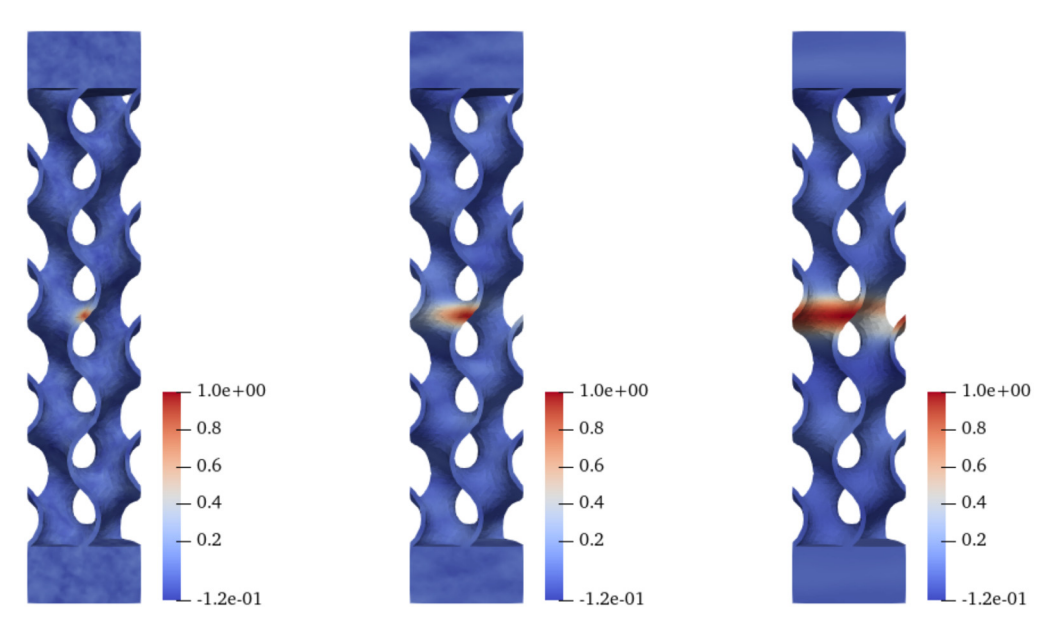


Fig. 5. Plot of the estimated correlation function of the Gaussian random field  $\{\Xi(x), x \in \Omega\}$  for  $\lambda = (\kappa^4/256, \kappa^4/256, \kappa^4/256)$  (quasi-isotropic kernel; left panel),  $\lambda = (\kappa^4/64, \kappa^4/64, \kappa^4/256)$  (moderately anisotropic kernel; middle panel), and  $\lambda = (\kappa^4/16, \kappa^4/16, \kappa^4/256)$  (strongly anisotropic kernel; right panel), with  $\kappa = 6$  [mm].

## 2.3. Definition of the transport map

We now turn to the definition of the transport map introducing non-Gaussianity in the model. Recall that the random field of material parameters is assumed to take the form

$$P(x) = \mathcal{T}(\Xi(x), x) , \quad \forall x \in \Omega , \tag{17}$$

where  $\mathcal{T}$  is such that  $P(x) \sim \pi$  (for x held fixed in  $\Omega$ ). It follows that the construction of the transport map is equivalent to the construction of an appropriate prior probability measure  $\pi$ . In this work, we build upon information theory to construct a least informative model. We specifically invoke the principle of maximum entropy, which states that amongst all probability density functions satisfying a set of constraints, such as the normalization condition, the best prior solution is the one that maximizes Shannon differential entropy. From a mathematical standpoint, this takes the form of a functional optimization problem, in which the solution is defined as

$$f = \arg\max_{g \in \mathcal{C}_{\pi}} H\{g\} , \tag{18}$$

where f is the probability density function associated with  $\pi$  (that is,  $\pi(d\mathbf{p}) = f(\mathbf{p})d\mathbf{p}$  with  $d\mathbf{p}$  the Lebesgue measure in  $\mathbb{R}^n$ ),  $\mathcal{C}_{\pi}$  denotes the set of admissible functions satisfying the aforementioned constraints, and  $H\{g\}$  is the Shannon entropy of g:

$$H\{g\} = \int_{\mathcal{S}} g(\boldsymbol{p}) \ln (g(\boldsymbol{p})) d\boldsymbol{p} , \qquad (19)$$

where S is taken as the support of the probability density function f. The constraints are written in vector form as

$$\mathbb{E}\{\Phi(P(x))\} = \phi , \qquad (20)$$

where  $\Phi$  is a vector-valued mapping encoding the information available on P(x) (recall that x is fixed) and  $\phi$  is a given vector. For instance, taking  $\Phi$  as the identity function implies that the mean value of P(x) is given. Likewise, defining  $\Phi$  as  $\Phi(p) = \text{vec}(p \otimes p)$ , where vec denotes the vectorization function, indicates that the correlation matrix of P(x) is known. By construction, the constraints to be accounted for, and hence the induced probability distribution, depends on the properties under investigation.

With a view towards the identification of the stochastic representation based on a set of structural experiments, we consider the modeling of the tensor-valued elasticity field, denoted by  $\{[\![C(x)]\!], x \in \Omega\}$ , in the following. Following the discussion in Section 2.2.1 (and more specifically, the adopted mesoscopic description), we assume that the random field is isotropic almost surely. In this case, the fourth-order elasticity tensor can be decomposed as

$$\llbracket C(x) \rrbracket = 3P_1(x) \llbracket J \rrbracket + 2P_2(x) \llbracket K \rrbracket , \quad \forall x \in \Omega , \tag{21}$$

where  $\{P_1(x), x \in \Omega\}$  and  $\{P_2(x), x \in \Omega\}$  are the random fields of bulk and shear moduli, and the tensor basis  $(\llbracket J \rrbracket, \llbracket K \rrbracket)$  for isotropic fourth-order tensors is defined as

$$[\![J]\!] = \frac{1}{3} [I_3] \otimes [I_3] , \quad [\![K]\!] = [\![I]\!] - [\![J]\!] ,$$
 (22)

with  $[I_3]$  and [I] the  $(3 \times 3)$  identity matrix and symmetrized fourth-order identity tensor, respectively.

Two modeling choices can be adopted at this stage. Following the seminal work [40] (see [20] for a unified treatment), one can assume that

$$\mathbb{E}\{\|C(x)\|\} = \|C\|, \quad \forall x \in \Omega, \tag{23}$$

and

$$\mathbb{E}\{\log\left(\det(\lceil C(x)\rceil)\right)\} = \chi \ , \quad |\chi| < +\infty \ , \quad \forall x \in \Omega \ , \tag{24}$$

where  $[\![C]\!]$  denotes the mean value of the elasticity field. Recall that this mean value is assumed constant due to identifiability constraints, following the discussion in Section 2.1. These constraints lead to a well-posed stochastic boundary value problem in elasticity, as proven in [40]. In this case, the moment information given by Eqs. (23) and (24) readily transfers to the elastic moduli, owing to the orthogonality of the tensor basis, and entropy maximization leads to two statistically independent random fields  $\{P_1(x), x \in \Omega\}$  and  $\{P_2(x), x \in \Omega\}$  that exhibit Gamma marginal distributions (see [20] for technical derivations):

$$P_1(\mathbf{x}) \sim \mathcal{G}(1/\delta_1^2, p_1 \delta_1^2) , \quad P_2(\mathbf{x}) \sim \mathcal{G}(1/\delta_2^2, p_2 \delta_2^2) ,$$
 (25)

where  $\mathcal{G}(h_1,h_2)$  denotes the Gamma probability distribution with shape and scale parameters given by  $h_1$  and  $h_2$ , respectively,  $\underline{p}_1$  and  $\underline{p}_2$  are the mean values of the bulk and shear moduli such that  $[\![\underline{C}]\!] = 3\underline{p}_1[\![J]\!] + 2\underline{p}_2[\![K]\!]$ , and  $\delta_1$  and  $\delta_2$  are the coefficients of variation of the two moduli. The transport map is then simply obtained as

$$P_i(\mathbf{x}) = \left(F_{\mathcal{G}(1/\delta_i^2, \underline{p}_i \delta_i^2)}^{-1} \circ F_{\mathcal{N}(0,1)}\right) (\Xi_i(\mathbf{x})) , \quad \forall \mathbf{x} \in \Omega , \quad i = 1, 2 ,$$

$$(26)$$

where  $F_{\mathcal{G}(h_1,h_2)}$  is the cumulative distribution function of the Gamma law with hyperparameters  $h_1$  and  $h_2$  (for later use, we denote by  $f_{\mathcal{G}(h_1,h_2)}$  the probability density function associated with this law),  $F_{\mathcal{N}(0,1)}$  is the cumulative distribution of the standard normal law, and the symbol  $\circ$  denotes function composition. This model is the least informative in that only mathematical information related to well-posedness is accounted for.

From a physical standpoint, the statistical independence of the two elastic moduli is, however, generally inconsistent with a multiscale interpretation where the moduli are often found to be highly correlated. In order to introduce pointwise correlation between the two moduli (at any location fixed in  $\Omega$ ), one can alternatively consider the construction of the joint distribution of P(x), based on the knowledge of the marginal laws associated with  $P_1(x)$  and  $P_2(x)$ . One possible choice consistent with the previous derivations is the use of a bivariate Gamma distribution. In what follows, we make use of the model proposed by Moran [41]:

$$f(\mathbf{p}) = \frac{1}{\sqrt{1 - \rho^2}} \exp\left\{-\frac{(\rho \tilde{p}_1)^2 - 2\rho \tilde{p}_1 \tilde{p}_2 + (\rho \tilde{p}_2)^2}{2(1 - \rho^2)}\right\} \prod_{i=1}^2 f_{\mathcal{G}(\delta_i^{-2}, \underline{p}_i \delta_i^2)}(p_i) , \qquad (27)$$

where  $\rho$  is the Pearson correlation coefficient between  $P_1(x)$  and  $P_2(x)$  at location  $x \in \Omega$ , and

$$\tilde{p}_i = \left(F_{\mathcal{N}(0,1)}^{-1} \circ F_{\mathcal{G}(1/\delta_i^2, p, \delta_i^2)}\right)(p_i) , \quad i = 1, 2 . \tag{28}$$

It can then be shown (see [41]) that

$$P_i(\mathbf{x}) = \left(F_{\mathcal{G}(1/\delta_i^2, \underline{P}_i, \delta_i^2)}^{-1} \circ F_{\mathcal{N}(0,1)}\right) (\Upsilon_i(\mathbf{x})) , \quad \forall \mathbf{x} \in \Omega , \quad i = 1, 2 ,$$

$$(29)$$

where  $\Upsilon(x) = (\Upsilon_1(x), \Upsilon_2(x))$  is a centered Gaussian random variable with covariance matrix

$$[C_{\Upsilon}] = \begin{bmatrix} 1 & \rho \\ \rho & 1 \end{bmatrix} . \tag{30}$$

The transport map can then be expressed in terms of  $\{\Xi(x), x \in \Omega\}$  through the Cholesky factorization of  $[C_{\Upsilon}]$ , leading to the generic representations

$$P_1(\mathbf{x}) = \left(F_{\mathcal{G}(1/\delta_1^2, \underline{p}_1 \delta_1^2)}^{-1} \circ F_{\mathcal{N}(0, 1)}\right) (\Xi_1(\mathbf{x})) , \quad \forall \mathbf{x} \in \Omega ,$$

$$(31)$$

and

$$P_2(\mathbf{x}) = \left(F_{\mathcal{G}(1/\delta_2^2, \underline{p}_2 \delta_2^2)}^{-1} \circ F_{\mathcal{N}(0,1)}\right) \left(\rho \Xi_1(\mathbf{x}) + \sqrt{1 - \rho^2} \Xi_2(\mathbf{x})\right) , \quad \forall \mathbf{x} \in \Omega ,$$

$$(32)$$

for an arbitrary value of  $\rho \in [-1, 1]$ .

Remark 2. The elasticity random field defined in Section 2.3 is isotropic almost surely and a few remarks regarding this modeling choice are relevant at this point. First, the level of anisotropy which is exhibited by AM materials is generally scale-dependent—the finer the scale, the more anisotropic the behavior. In this work, we consider a mesoscopic resolution aggregating fluctuations over multiple layers, each of which corresponding to a rotated laser path. As noticed earlier, this leads to an isotropization of the mesoscopic fields in a way that is similar to what is observed on layered composites made up with unidirectional plies. Second, moderately anisotropic fields may reasonably be well approximated by isotropic representations (if the former is available, the latter may be computed through projections in relevant tensor spaces; see [42] and the references therein), especially when quantities of interest are defined at coarser scales (here, the structural scale). Third, the proposed derivations can readily be extended to anisotropic elastic behaviors using the transport maps proposed in [43], where the elasticity random field is decomposed as

$$[\![C(x)]\!] = [\![M(x)]\!]^{1/2} [\![A(x)]\!] [\![M(x)]\!]^{1/2} , \quad \forall x \in \Omega ,$$
(33)

where  $\{[\![M(x)]\!], x \in \Omega\}$  and  $\{[\![A(x)]\!], x \in \Omega\}$  are two auxiliary random fields exhibiting fluctuations in a material class of interest (see [20]) and in the triclinic class (see [40]), respectively. Proceeding as in Section 2.1, each field can be written as

$$[\![M(x)]\!] = \mathcal{T}_M(\Xi_M(x), x) , \quad \forall x \in \Omega , \tag{34}$$

$$[\![A(x)]\!] = \mathcal{T}_A(\Xi_A(x), x) , \quad \forall x \in \Omega , \tag{35}$$

where the vector-valued Gaussian random fields  $\{\Xi_M(x), x \in \Omega\}$  and  $\{\Xi_A(x), x \in \Omega\}$  are defined following the derivations in Section 2.2, and the transport maps  $\mathcal{T}_M$  and  $\mathcal{T}_A$  are deduced from the information-theoretic formulation (as explained in [20,40]). The benefit of this model is that the representation allows for the level of statistical fluctuations to be decoupled from the level of anisotropy. The calibration of such representations, however, requires rich experiments—typically, full-field measurements at the modeling scale—that are not considered in this paper.

**Remark 3.** As previously indicated, the proposed stochastic modeling framework can be used to model other material parameters on AM structures, depending on the application and the availability of experimental data (to perform model identification and to discuss validation aspects). In a plasticity model for instance, a spatially-varying yield stress, denoted by  $\{\Sigma_Y(x), x \in \Omega\}$ , can be represented in the form

$$\Sigma_{Y}(\mathbf{x}) = \mathcal{T}(\Xi(\mathbf{x}), \mathbf{x}) , \quad \forall \mathbf{x} \in \Omega ,$$
 (36)

where  $\{\Xi(x), x \in \Omega\}$  is the scalar Gaussian random field defined in Section 2.2, and  $\mathcal{T}$  is an appropriate transport map pushing the Gaussian measure forward. Since the yield stress is positive almost surely, the approach presented in Section 2.3 can be deployed under the constraint  $\mathbb{E}\{\Sigma_Y(x)\}=\underline{\sigma}_Y$  for any x in  $\Omega$ , with  $\underline{\sigma}_Y>0$  the desired mean value for the yield stress. Taking  $(0,+\infty)$  as the support of the first-order marginal probability density function, it can be deduced that a possible information-theoretic model is

$$\Sigma_{Y}(\mathbf{x}) = \left(F_{\operatorname{Exp}(1/\sigma_{Y})}^{-1} \circ F_{\mathcal{N}(0,1)}\right) (\Xi(\mathbf{x})) , \quad \forall \mathbf{x} \in \Omega ,$$
(37)



Fig. 6. As-printed Ti LPBF gyroid sample.

where  $F_{\text{Exp}(1/\underline{\sigma}_Y)}$  the cumulative distribution function of the exponential law with rate parameter  $1/\underline{\sigma}_Y$ . Note that in this case, the yield stress random field is of second-order and exhibits a marginal variance given by  $1/\underline{\sigma}_Y^2$ . Additional modeling flexibility can be obtained by supplementing the aforementioned constraint in mean (that is,  $\mathbb{E}\{\Sigma_Y(x)\} = \underline{\sigma}_Y$ ) by the constraint  $\mathbb{E}\{\log(\Sigma_Y(x))\} = \chi$ , with  $|\chi| < +\infty$ , in which case the information-theoretic formulation yields

$$\Sigma_{Y}(\mathbf{x}) = \left(F_{\mathcal{G}(1/\delta_{Y}^{2},\underline{\sigma}_{Y}\delta_{Y}^{2})}^{-1} \circ F_{\mathcal{N}(0,1)}\right)(\Xi(\mathbf{x})) , \quad \forall \mathbf{x} \in \Omega ,$$
(38)

where  $\delta_Y$  is the marginal coefficient of variation of  $\Sigma_Y(x)$ , for all x in  $\Omega$ .

## 3. Model identification and validation based on physical experiments

In this section, we address the identification of model parameters based on a set of structural experiments on 3D printed scaffolds. The material processing conditions and experimental setups are first described in Section 3.1. The experimental results are discussed in Section 3.2. The calibration and validation strategies are finally presented in Sections 3.3 and 3.4, respectively.

## 3.1. Material processing and experimental setup

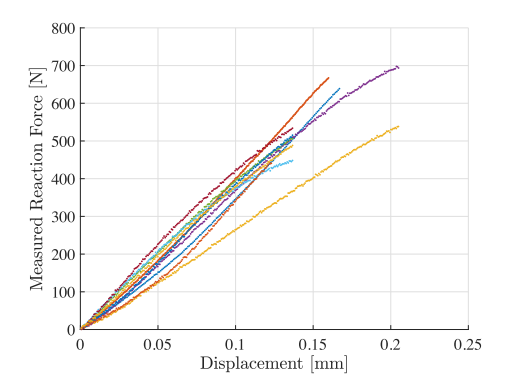
Additive manufacturing provides a new alternative method for the treatment of large orthopaedic defects. Laser powder bed fusion allows for the fabrication of patient-specific anatomic metal implants with complex porous architectures [44]. The porous gyroid architecture allows for bone to grow into the scaffold, facilitating osseointegration while providing mechanical stability. The implementation of large porous 3D metal implants is relatively new and the long-term clinical outcomes are understudied [45]. FE modeling techniques can be used to safely and efficiently evaluate printed structures to optimize implants and improve surgical outcomes.

The experimental tests were designed to represent common stresses seen by 3D printed implants. Test samples were printed via LPBF using a 3D Systems ProX DMP320 system with medical grade titanium alloy powder (Ti6Al4V), the most common material in 3D printed implant [46]. The printing powder has a spherical morphology with an average diameter of 35 [ $\mu$ m], conforming with chemistry appropriate for implanted medical device per ASTM F3001. The test samples in Fig. 6 were designed to be compatible for loading under multiple stress states, including compression, torsion, and bending tests, all being relevant loading mechanisms for large metal implants. The gage section on the samples had a diameter of 6 [mm] and length of 24 [mm]. Experimental compressive and torsion tests were conducted using a Test Resources 830 loading frame, at a constant axial displacement of 1 [mm/min] or rotation of 30 [deg/min] until failure.

#### 3.2. Data processing for calibration and validation

The experimental results for the compression and torsion tests are shown in Figs. 7 and 8, respectively. In these figures, the subfigures in the left panels display raw data in the linear elastic regime, while the subfigures in the right panels show linear regression results on these data. It is seen that both sets of results exhibit large variability, and that the data related to the torsion test present substantial noise.

Based on these results, reaction forces and torques are evaluated for all samples, for the same loading condition. Specifically, reactions are estimated for a prescribed displacement  $u_D = -0.1230$  [mm], while torques are computed from the loading curves for a prescribed twist angle  $\gamma = 0.1132$  [rad]. The values thus obtained are reported in



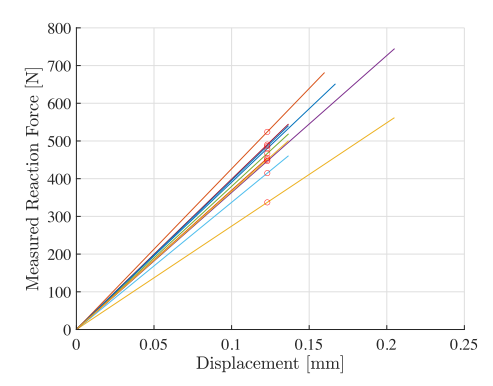
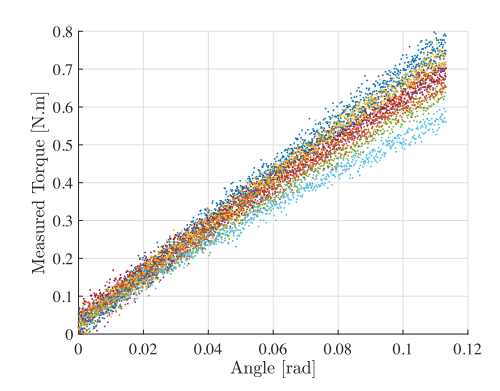


Fig. 7. Experimental results for the compression tests: Raw data (left) and linear regression results (right). Red circles in the right panel indicate points where reaction forces are evaluated.



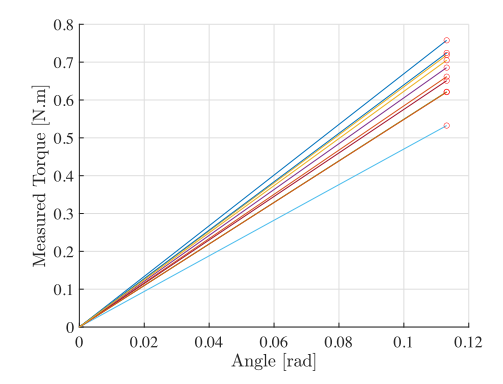


Fig. 8. Experimental results for the torsion tests: Raw data (left) and linear regression results (right). Red circles in the right panel indicate points where torques are evaluated.

**Table 1** Realizations of the reaction force and torque measured in the compression tests (for a prescribed displacement  $u_D = -0.1230$  [mm]) and torsion tests (for a prescribed twist angle  $\gamma = 0.1132$  [rad]), respectively.

Sample #	Compression test: Reaction force in [N]	Torsion test: Torque in [N m]
1	480.1134	0.7577
2	524.1933	0.6616
3	337.1690	0.7187
4	446.8893	0.6856
5	466.8420	0.6217
6	414.7078	0.5325
7	490.4148	0.6510
8	486.4872	0.7244
9	454.3928	0.6207
10	450.5290	0.7050

Table 1. The mean values for the experimental reaction force and torque are given by  $\underline{R}^{\text{exp}} = 455.1739$  [N] and  $\underline{T}^{\text{exp}} = 0.6679$  [N m], respectively. In addition, the coefficients of variation for these quantities are estimated to  $\delta_R^{\text{exp}} = 0.1120$  and  $\delta_T^{\text{exp}} = 0.0980$  (notice, however, that the number of samples is too small to obtain converged statistical estimators).

## 3.3. Methodology for model calibration

We now seek to identify the hyperparameters defining the random fields of bulk and shear moduli. Recall that these non-Gaussian fields are the two components of the vector-valued random field  $\{P(x), x \in \Omega\}$  defined as (see Section 2.1)

$$P(x) = \mathcal{T}(\Xi(x)) , \tag{39}$$

where the transport map is defined through the information-theoretic model described in Section 2.3. In accordance with multiscale observations, we assume in this work that the two elastic moduli are fully correlated at any location in  $\Omega$ . Taking  $\rho = 1$  then yields

$$P(x) = \mathcal{T}(\Xi_1(x)) \tag{40}$$

and

$$P_i(\mathbf{x}) = \left(F_{\mathcal{G}(1/\delta_i^2, \underline{p}, \delta_i^2)}^{-1} \circ F_{\mathcal{N}(0,1)}\right) (\Xi_1(\mathbf{x})) , \quad \forall \mathbf{x} \in \Omega , \quad i = 1, 2 .$$

$$(41)$$

The stochastic model is hence parameterized by six hyperparameters, namely

- the mean values  $p_1$  and  $p_2$  for the bulk and shear moduli;
- ullet the coefficients of variation  $\delta_1$  and  $\delta_2$  for the bulk and shear moduli; and
- the parameters  $\kappa$  and  $\lambda$  defining the underlying Gaussian field  $\{\Xi_1(x), x \in \Omega\}$  through the SPDE (see Eqs. (4) and (5)).

In order to reduce the number of parameters, we formulate the following assumptions.

- The mean values  $\underline{p}_1$  and  $\underline{p}_2$  are parameterized by the mean value of the Young's modulus, denoted by  $\underline{E}$ , with a value of Poisson ratio fixed to 0.342.
- The bulk and shear moduli random fields exhibit the same level of fluctuations, and we set  $\delta_1 = \delta_2 =: \delta$ . Note that in this case, the Poisson ratio is indeed constant (on the contrary, the Poisson ratio is stochastic and spatially varying when  $\delta_1 \neq \delta_2$ ).
- The global correlation range parameter  $\kappa$  is set to the smallest characteristic dimension of the sample, which is the diameter of the cylindrical geometry:  $\kappa = 6$  [mm].
- Based on both the processing conditions and scale of description, the in-plane parameters for the correlation structure are assumed equal:  $\lambda_1 = \lambda_2 =: \lambda_{12}$ .

In addition, we define the change of variables  $L_{12} = \sqrt{\lambda_{12}}/\kappa$  and  $L_3 = \sqrt{\lambda_3}/\kappa$ , where  $L_{12}$  and  $L_3$  are interpreted as correlation lengths (see [20]). Let  $\mathbf{w} = (\underline{E}, \delta, L_{12}, L_3)^\mathsf{T}$  be the vector of all remaining hyperparameters, and denote by  $S_{\mathbf{w}} \subset \mathbb{R}^4$  its admissible set.

**Remark 4.** In this work, we do not address the identification of the functional forms for the correlation functions as the calibration is based on structural responses that are typically insensitive to this modeling choice (but remain fairly sensitive to correlation lengths). When data can be obtained at mesoscale, through full-field measurements for instance, the parameter  $\alpha$  controlling the smoothness of the realizations (as implied by mean-square differentiability) may be identified as well to find an optimal solution within the whole class of Matérn covariance functions (see also [20] for an updating strategy to search for a solution outside that class).

In order to proceed with the identification of the model, we introduce the stochastic boundary value problem (SBVP):

$$\begin{cases} \operatorname{div}([\boldsymbol{\Sigma}]) = \mathbf{0} , & \forall x \in \Omega , \\ [\boldsymbol{\Sigma}(x)] = [\![\boldsymbol{C}_{w}(x)]\!] : [\boldsymbol{\mathcal{E}}(x)] , & \forall x \in \Omega , \\ [\boldsymbol{\mathcal{E}}(x)] = \nabla_{x}^{S} u(x) , & \forall x \in \Omega , \end{cases}$$

$$(42)$$

where  $[\Sigma]$  is the Cauchy stress tensor,  $[\mathcal{E}]$  is the linearized strain tensor, the symbol  $\nabla_x^S$  denotes the symmetrized gradient operator,  $\boldsymbol{u}=(u_1,u_2,u_3)^T$  is the displacement vector, and  $\{[\![\boldsymbol{C}_w(x)]\!],x\in\Omega\}$  is the elasticity random field defined as

$$[\![C_{w}(x)]\!] = 3P_{1}(x; w)[\![J]\!] + 2P_{2}(x; w)[\![K]\!], \quad \forall x \in \Omega,$$
(43)



Fig. 9.  $\mathbb{P}_2$  tetrahedral mesh used in the stochastic finite element formulation.

where the random fields of elastic moduli are defined in Section 2 and the dependence on  $\boldsymbol{w}$  is made explicit. The problem stated in Eq. (42) is supplemented with appropriate boundary conditions to mimic the physical experiments described in Section 3.1. We define the two following SBVPs.

• SBVP-1 corresponds to the compression experiment. In this case, Eq. (42) is supplemented with the Dirichlet boundary conditions

$$u_3 = u_D \text{ on } \partial \Omega_{\text{top}}, \quad \boldsymbol{u} = \boldsymbol{0} \text{ on } \partial \Omega_{\text{bottom}},$$
 (44)

where  $\partial \Omega_{\text{top}}$  and  $\partial \Omega_{\text{bottom}}$  denote the top and bottom surface boundaries of the sample, respectively, and  $u_D = -0.1230$  [mm] (as indicated in Section 3.2).

• SBVP-2 is associated with the torsion test, so Eq. (42) is complemented with the Dirichlet boundary conditions

$$\mathbf{u} = (\gamma x_2, -\gamma x_1, 0)^{\mathsf{T}} \text{ on } \partial \Omega_{\text{top}} , \quad \mathbf{u} = \mathbf{0} \text{ on } \partial \Omega_{\text{bottom}} ,$$
 (45)

with  $\gamma = 0.1132$  [rad] (see Section 3.2).

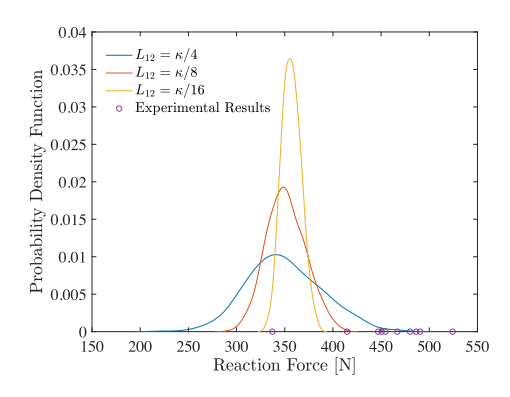
The identification of the model is carried out by propagating the material uncertainties by means of the stochastic finite element method (with a Monte Carlo stochastic solver). Specifically, for a fixed value of  $\mathbf{w}$  and for each realization of the random fields, the solutions to the two SBVPs are obtained by using a  $\mathbb{P}_2$  tetrahedral mesh with 354,190 nodes and 208,185 elements (with characteristic element size h=0.18 [mm]; see Fig. 9). Samples of the stochastic reaction force are then collected by numerically integrating the relevant stress component over  $\partial \Omega_{\text{top}}$ , using a stress recovery procedure and the solution to SBVP-1. We denote this stochastic reaction force (along  $e^3$ ) by  $R_{\mathbf{w}}$ . Likewise, realizations of the stochastic torque, which is denoted by  $T_{\mathbf{w}}$  below, are computed by integrating the elemental torque contributions over  $\partial \Omega_{\text{top}}$  provided by the solution to SBVP-2.

Several strategies can be pursued to compute an optimal value  $\mathbf{w}^{\text{opt}}$  of  $\mathbf{w}$ , including the use of a least-square method (where the discrepancy in second-order moments is minimized), the maximum likelihood method, or a Bayesian approach, to list a few. The choice of a relevant approach is guided, in practice, by the availability of experimental results, as well as by the nature of the hyperparameters to be identified. In this work, we rely on the maximum likelihood method, given data limitations, and we thus define the optimal hyperparameter as

$$\boldsymbol{w}^{\text{opt}} = \arg \max_{\boldsymbol{w} \in \mathcal{S}_{\boldsymbol{w}}} \ \mathcal{J}(\boldsymbol{w}) \ , \tag{46}$$

where the cost function  $\mathcal{J}$  is given by

$$\mathcal{J}(\boldsymbol{w}) = \sum_{i=1}^{N^{\text{exp}}} \ln\{\hat{f}_{R_{\boldsymbol{w}}}(R^{\text{exp}}(\theta_i))\hat{f}_{T_{\boldsymbol{w}}}(T^{\text{exp}}(\theta_i))\}, \qquad (47)$$



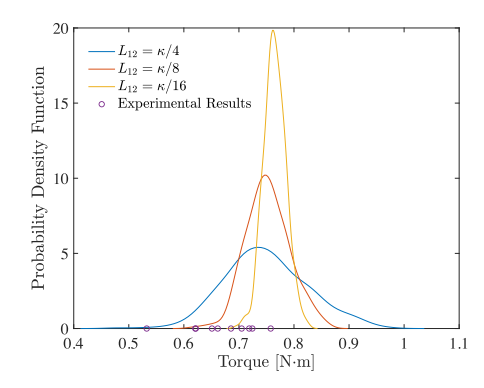


Fig. 10. Probability density functions of the stochastic reaction force (left) and torque (right), estimated with 480 independent samples, for  $\underline{E} = 128$  [GPa],  $\delta = 0.4$ ,  $\kappa = 6$  [mm], and different values of correlation parameters  $L_{12}$  and  $L_{3}$ .

where  $\hat{f}_{R_w}$  and  $\hat{f}_{T_w}$  are the probability density functions of the stochastic reaction force and torque, obtained with the computational model parameterized by  $\boldsymbol{w}$  through a kernel density estimation, and  $\{R^{\exp}(\theta_i)\}_{i=1}^{N^{\exp}}\}$  and  $\{T^{\exp}(\theta_i)\}_{i=1}^{N^{\exp}}\}$  are the experimentation realizations of the reaction force and torque (with  $N^{\exp}=10$ ; see Table 1). The above optimization problem is non-convex and is solved by searching the optimal solution over a predefined grid in the search space. In order to gain insight about (i) the most influential variables for each mechanical test, and (ii) the definition of bounds—and increments—in the search space, sensitivity analyses were conducted for the two SBVPs. The evolution of the probability density functions for the stochastic reaction force and torque as a function of correlation length parameters is shown in Fig. 10 for instance.

In general, it was observed that

- the distribution of the reaction force is mostly sensitive to  $\underline{E}$ ,  $\delta$ , and  $L_3$  (which affects the spatial variations along the longitudinal direction of the samples);
- the distribution of the stochastic torque is mostly affected by  $\underline{E}$ ,  $\delta$ , and  $L_{12}$  (which qualitatively controls the frequency of the oscillations in the transverse plane); and that
- the larger the correlation lengths, the larger the levels of statistical fluctuations for the reaction force and torque—with a minor, yet noticeable effect on the mean values for these quantities of interest.

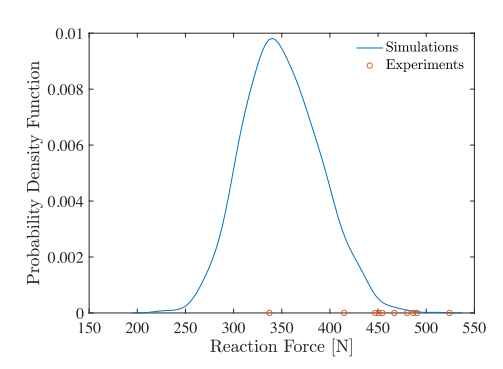
Based on these qualitative sensitivity results, the search was completed by considering the following sets of trial parameters:  $\underline{E} \in \{103, 114, 125, 128, 130\}$  [GPa],  $\delta \in \{0.1, 0.2, 0.3, 0.4\}$ ,  $L_{12} \in \{\kappa/32, \kappa/16, \kappa/8, \kappa/4\}$ , and  $L_3 \in \{\kappa/32, \kappa/16, \kappa/8, \kappa/4\}$  (note that this choice of correlation lengths in consistent with the density of the finite element mesh, which has a characteristic size of 0.18 [mm] and enables the proper discretization of the stochastic fields). This represents a set of 320 combinations to be tested, and we consider 480 realizations for each BVP to ensure reasonable convergence in the estimation of the probability density functions, as well as moderate computational cost. Each scenario therefore necessitates solving  $2 \times 480 = 960$  boundary value problems. Typical computational times (for one scenario) are reported below for an implementation in C and parallel execution (whenever possible) on 24 cores (Intel Xeon Gold 3 GHz processor):

- Computing the diffusion field through the Laplace problem: 2 [s].
- Sampling the realizations for the underlying Gaussian field (480 realizations): 50 [s].
- Computing the realizations for the non-Gaussian fields (480 realizations): 74 [s].
- Solving the 2 stochastic finite element problems: 20 [h].

It should be noticed at this point that the resolution at which the solution is sought in the admissible set  $S_w$  is strongly affected by the nature of the experimental results, which are essentially relevant to the effective response of the structure. This constitutes a severe limitation for the identification of the random field representation that intrinsically captures fluctuations of material properties at the mesoscale, for minor variations in the hyperparameters lead to indistinguishable effects at the macroscopic level.

The optimal solution over the aforementioned grid was obtained as

$$\underline{E} = 128 \; , \quad \delta = 0.4 \; , \quad L_{12} = L_3 = \kappa/4 \; . \tag{48}$$



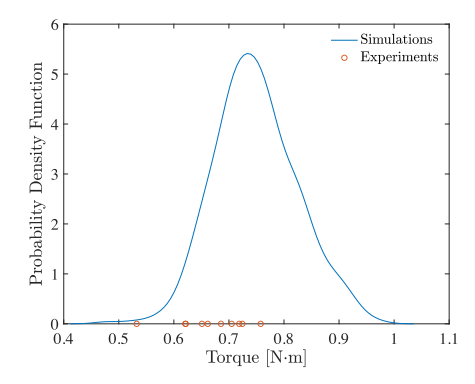


Fig. 11. Probability density function of the stochastic reaction force (left) and torque (right) obtained with the computational model and the calibrated random field representation (solid line) and experimental realizations (red circle).

The mean value for the Young's modulus belongs to the range of values that are typically reported for titanium. The coefficient of variation  $\delta$  is much larger than the levels of fluctuations observed at the structural level (which is about ten percents), which is expected given the transition between the mesoscopic and macroscopic scales. The identified in-plane correlation range implies that the elasticity field is indeed spatially correlated over almost the entire cross-section of the samples, which is consistent with the underlying manufacturing process. Finally, it is found that a quasi-isotropic correlation structure (that is,  $L_{12} = L_3$ ) provides a better agreement with the experiments, suggesting that the multi-physical processes arising sequentially in the AM technique (namely, in-plane filling and stacking along the third orthogonal direction) generate similar spatial memory in terms of characteristic length scales.

A comparison between the probability density functions obtained with these parameters and the set of experimental data is shown in Fig. 11 for both the compression tests and torsion experiments. It is seen that the experimental realizations have non-vanishing probability levels for the probability distributions estimated with the calibrated stochastic model. The latter captures the mean value for the stochastic torque fairly well, while the stochastic prediction underestimates the mean for the compression experiments. Specifically, the mean values for the simulation-based stochastic reaction force and torque are  $\underline{R}^{\text{sim}} = 349.8504$  [N] and  $\underline{T}^{\text{sim}} = 0.7497$  [N m], respectively. The relative errors between these mean values and the mean values estimated from the experiments are 23% and 12%, respectively.

## 3.4. Validation

In order to discuss validation with an independent set of data, additional experiments were conducted on the same material and structure. Specifically, 3-point bending was done using Material Testing System (MTS) Criterion<sup>®</sup> Series 43. A 3-point bending fixture was attached to MTS with the loading roller centered between the support roller that were 60 [mm] apart (see Fig. 12). The test sample was orientated and placed on the support rollers so the loading roller was above the same feature on the gyroid as the FE model. The samples were loaded in 3-point bending at a constant displacement rate of 25.4 [mm/min] until a fracture occurred. The reaction force was measured by a 50 [kN] load cell above the loading roller.

The experimental results for the bending tests are shown in Fig. 13, where raw data and linear regression results are displayed. The realizations of the reaction force are estimated for a transverse displacement  $u_D = -1.4816$  [mm] and are reported in Table 2. The mean value for the experimental reaction force in the 3-point bending test is 56.2772 [N], with a coefficient of variation estimated to 0.0480.

In order to compare model predictions, we then consider a third stochastic boundary value problem (SBVP-3) in which Eq. (42) is supplemented with the Dirichlet boundary conditions:

$$u_3(\mathbf{x}_{top}) = u_D$$
,  $\mathbf{u} = \mathbf{0}$  on  $\partial \Omega_{bottom}$ , (49)

where  $x_{\text{top}}$  is the point of contact for the transverse displacement actuator, located on the upper surface of the sample (see Fig. 12),  $\partial \Omega_{\text{bottom}}$  gathers the two lines of contact located on the lower surface of the sample (see Fig. 12), and  $u_D = -1.4816$  [mm].

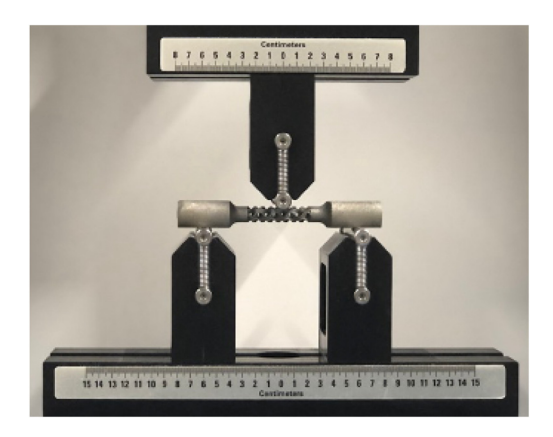


Fig. 12. Experimental setup for the 3-point bending test.

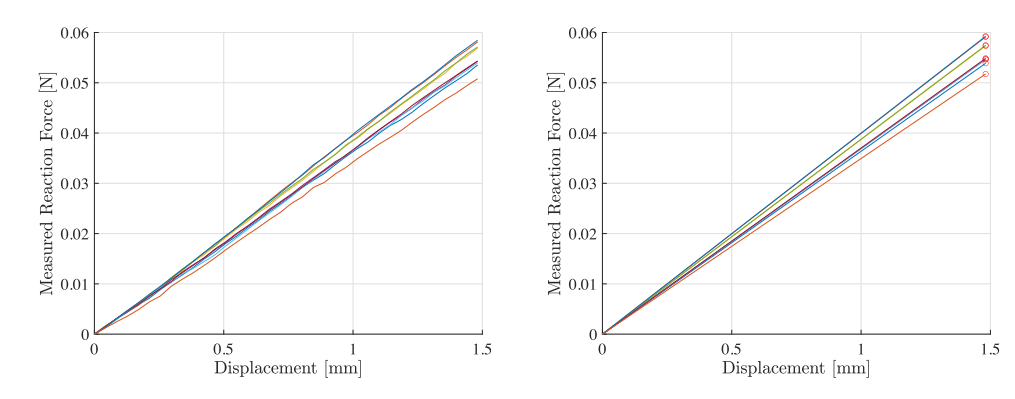


Fig. 13. Experimental results for the bending tests: Raw data (left) and linear regression results (right). Red circles in the right panel indicate points where torques are evaluated.

**Table 2** Reaction forces measured in 3-point bending tests (for a prescribed transverse displacement  $u_D = -1.4816$  [mm]).

Sample #	Bending test: Reaction force in [N]
1	59.8130
2	53.8757
3	59.1379
4	57.3504
5	54.6463
6	57.4529
7	54.6614
8	54.8524
9	59.2355
10	51.7467

A comparison between the probability density function obtained with the calibrated hyperparameters and the experimental data is shown in Fig. 14. As with the compression and torsion tests, it is observed that the experimental realizations associated with the 3-point bending experiments have non-vanishing probability levels for the probability distributions estimated with the calibrated stochastic model. The computational results overestimate the mean value, with a relative error of about 20%. A few important comments regarding the identification and validation results are in order.

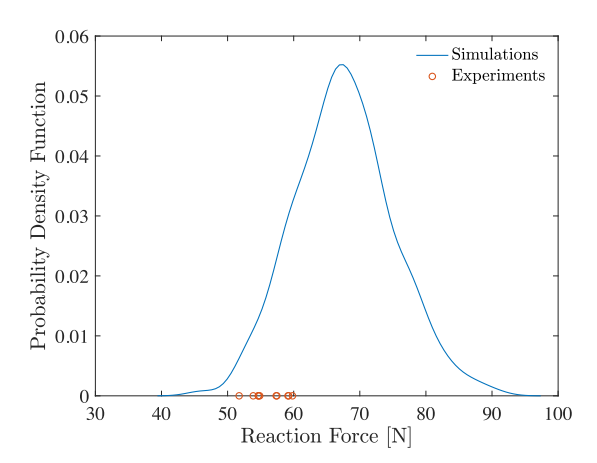


Fig. 14. Validation results based on the bending experiments: Probability density function of the stochastic reaction force obtained with the computational model and the calibrated random field representation (solid line) and experimental realizations (red circle).

- First of all, it should be stressed that the quantities of interests involved in the inverse problem are very sensitive to the applied boundary conditions: variations in the order of 0.01 [mm] can lead to a substantial shift in the mean value for the compression tests, for instance.
- Experimental results were fed into the computational model without specific postprocessing. The use of a Bayesian approach to account for potential noise is a natural extension of the present work where the calibrated probabilistic representation could be used as a prior model.
- The identification procedure implicitly assumes that the designed structure (which is used in the computational model) and the as-produced geometry coincide perfectly. This, indeed, represents a major assumption, since geometrical deviations are often observed on AM structures [47,48] and may play a critical role for highly porous structures (for which variations in the order of 0.1% in porosity can lead to variations of a few tens of newtons in reaction forces, for instance). In this context, the combination of the proposed stochastic formulation with a suitable representation for geometrical uncertainties constitutes a valuable path that will be explored in future works.
- As previously indicated, the consideration of two different scales to perform modeling and identification
  inevitably leads to a lack of sensitivity with respect to some hyperparameters. In addition, competing behavior
  can be observed while optimizing with respect to a set of experiments. Here, the integration of multiscale observations shall be pursued in an attempt to circumvent under-determination for spatially-dependent
  constitutive parameters.

#### 4. Conclusion

In this work, we proposed a stochastic framework for the representation, simulation, and identification of non-Gaussian random fields of material properties on complex geometries. A generic modeling approach was first laid down. This approach builds on the definition of a stochastic partial differential equation, which is introduced on purpose to capture the complex features of the AM part on the fly, and on information-theoretic measure transports, aimed to ensure well-posedness in the associated stochastic boundary value problem. An application to the modeling of mesoscopic elasticity tensors on structures produced by additive manufacturing was specifically presented. An isotropic approximation was considered to that end, and model identification and validation were tackled by considering a set of physical experiments on titanium scaffolds, produced by laser powder bed fusion. While quantities of interest exhibit high sensitivity to model parameters, including boundary conditions and nominal geometry, it was shown that the calibrated stochastic model has the ability to generate non-vanishing probability levels for all experimental observations.

## **Declaration of competing interest**

The authors declare that they have no known competing financial interests or personal relationships that could have appeared to influence the work reported in this paper.

## Acknowledgments

The work of S.C. and J.G. was partially supported by the National Science Foundation, USA, Division of Civil, Mechanical and Manufacturing Innovation, under awards CMMI-1726403 and CMMI-1942928.

#### References

- [1] Zhen Hu, Sankaran Mahadevan, Uncertainty quantification and management in additive manufacturing: current status, needs, and opportunities, Int. J. Adv. Manuf. Technol. 93 (5) (2017) 2855–2874.
- [2] Chandrika Kamath, Data mining and statistical inference in selective laser melting, Int. J. Adv. Manuf. Technol. 86 (5) (2016) 1659–1677.
- [3] Jordi Delgado, Joaquim Ciurana, Ciro A. Rodríguez, Influence of process parameters on part quality and mechanical properties for DMLS and SLM with iron-based materials, Int. J. Adv. Manuf. Technol. 60 (5–8) (2012) 601–610.
- [4] N. Raghunath, Pulak M. Pandey, Improving accuracy through shrinkage modelling by using Taguchi method in selective laser sintering, Int. J. Mach. Tools Manuf. 47 (6) (2007) 985–995.
- [5] P. Nath, Z. Hu, S. Mahadevan, Multi-level uncertainty quantification in additive manufacturing, in: Solid Freeform Fabrication 2017: Proceedings of the 28th Annual International Solid Freeform Fabrication Symposium – An Additive Manufacturing Conference, 2017, pp. 922–937.
- [6] Gustavo Tapia, Wayne King, Luke Johnson, Raymundo Arroyave, Ibrahim Karaman, Alaa Elwany, Uncertainty propagation analysis of computational models in laser powder bed fusion additive manufacturing using polynomial chaos expansions, J. Manuf. Sci. Eng. 140 (2018) 121006.
- [7] Tesfaye Moges, Gaurav Ameta, Paul Witherell, A review of model inaccuracy and parameter uncertainty in laser powder bed fusion models and simulations, J. Manuf. Sci. Eng. 141 (2019) http://dx.doi.org/10.1115/1.4042789.
- [8] Gregory Thomas Loughnane, A framework for uncertainty quantification in microstructural characterization with application to additive manufacturing of Ti-6Al-4V, 2015.
- [9] Guowei Cai, Sankaran Mahadevan, Uncertainty quantification of manufacturing process effects on macroscale material properties, Int. J. Multiscale Comput. Eng. 14 (3) (2016).
- [10] Felipe Lopez, Paul Witherell, Brandon Lane, Identifying uncertainty in laser powder bed fusion additive manufacturing models, J. Mech. Des. 138 (11) (2016).
- [11] Supriyo Ghosh, Mohamad Mahmoudi, Luke Johnson, Alaa Elwany, Raymundo Arroyave, Douglas Allaire, Uncertainty analysis of microsegregation during laser powder bed fusion, Modelling Simulation Mater. Sci. Eng. 27 (3) (2019) 034002.
- [12] Supriyo Ghosh, Raiyan Seede, Jaylen James, Ibrahim Karaman, Alaa Elwany, Douglas Allaire, Raymundo Arroyave, Statistical modelling of microsegregation in laser powder-bed fusion, Phil. Mag. Lett. 100 (6) (2020) 271–282.
- [13] Zhuo Wang, Chen Jiang, Pengwei Liu, Wenhua Yang, Ying Zhao, Mark F. Horstemeyer, Long-Qing Chen, Zhen Hu, Lei Chen, Uncertainty quantification and reduction in metal additive manufacturing, npj Comput. Mater. 6 (1) (2020) 175.
- [14] Zhuo Wang, Pengwei Liu, Yanzhou Ji, Sankaran Mahadevan, Mark F. Horstemeyer, Zhen Hu, Lei Chen, Long-Qing Chen, Uncertainty quantification in metallic additive manufacturing through physics-informed data-driven modeling, J. Miner. Met. Mater. Soc. 71 (8) (2019) 2625–2634.
- [15] Thirupathi Maloth, Deniz Ozturk, Garrison M. Hommer, Adam L. Pilchak, Aaron P. Stebner, Somnath Ghosh, Multiscale modeling of cruciform dwell tests with the uncertainty-quantified parametrically homogenized constitutive model, Acta Mater. 200 (2020) 893–907.
- [16] David Garcia, Ziling Wu, Jee Yun Kim, Z. Yu Hang, Yunhui Zhu, Heterogeneous materials design in additive manufacturing: Model calibration and uncertainty-guided model selection, Addit. Manuf. 27 (2019) 61–71.
- [17] R. Ghanem, D. Higdon, H. Owhadi, Handbook of Uncertainty Quantification, Springer, Cham, 2017.
- [18] C. Scarth, S. Adhikari, P. Higino Cabral, G.H.C. Silva, A. Pereira do Prado, Random field simulation over curved surfaces: Applications to computational structural mechanics, Comput. Methods Appl. Mech. Engrg. 345 (2019) 283–301.
- [19] Brian Staber, Johann Guilleminot, A random field model for anisotropic strain energy functions and its application for uncertainty quantification in vascular mechanics, Comput. Methods Appl. Mech. Engrg. 333 (2018) 94–113.
- [20] B. Staber, J. Guilleminot, Stochastic modeling and generation of random fields of elasticity tensors: A unified information-theoretic approach, C. R. Méc. 345 (6) (2017) 399–416.
- [21] Shanshan Chu, Johann Guilleminot, Stochastic multiscale modeling with random fields of material properties defined on nonconvex domains, Mech. Res. Commun. 97 (2019) 39–45.
- [22] P. Whittle, On stationary processes in the plane, Biometrika 41 (3-4) (1954) 434-449.
- [23] P. Whittle, Stochastic processes in several dimensions, Bull. Int. Stat. Inst. 40 (1963) 974–994.
- [24] F. Lindgren, H. Rue, J. Lindström, An explicit link between Gaussian fields and Gaussian Markov random fields: the stochastic partial differential equation approach, J. R. Stat. Soc. Ser. B Stat. Methodol. 73 (4) (2011) 423–498.
- [25] Lassi Roininen, Janne M.J. Huttunen, Sari Lasanen, Whittle-Matérn priors for Bayesian statistical inversion with applications in electrical impedance tomography, Inverse Probl. Imaging 8 (2) (2014) 561–586.

- [26] Matthew M. Dunlop, Andrew M. Stuart, The Bayesian formulation of EIT: Analysis and algorithms, Inverse Probl. Imaging 10 (4) (2016) 1007–1036.
- [27] Per Sidén, Anders Eklund, David Bolin, Mattias Villani, Fast Bayesian whole-brain fMRI analysis with spatial 3D priors, NeuroImage 146 (2017) 211–225.
- [28] Lassi Roininen, Mark Girolami, Sari Lasanen, Markku Markkanen, Hyperpriors for Matérn fields with applications in Bayesian inversion, Inverse Probl. Imaging 13 (1) (2019) 1–29.
- [29] Per Sidén, Finn Lindgren, David Bolin, Anders Eklund, Mattias Villani, Spatial 3D Matérn priors for fast whole-brain fMRI analysis, 2019.
- [30] Amanda F. Mejia, Yu (Ryan) Yue, David Bolin, Finn Lindgren, Martin A. Lindquist, A Bayesian general linear modeling approach to cortical surface fMRI data analysis, J. Amer. Statist. Assoc. 115 (530) (2020) 501–520.
- [31] David Bolin, Finn Lindgren, Spatial models generated by nested stochastic partial differential equations, with an application to global ozone mapping, Ann. Appl. Stat. 5 (1) (2011) 523–550.
- [32] Johann Guilleminot, Alireza Asadpoure, Mazdak Tootkaboni, Topology optimization under topologically dependent material uncertainties, Struct. Multidiscip. Optim. 60 (2019) 1283–1287.
- [33] Peng Chen, Michael R. Haberman, Omar Ghattas, Optimal design of acoustic metamaterial cloaks under uncertainty, J. Comput. Phys. 341 (2021) 110114.
- [34] Yair Daon, Georg Stadler, Mitigating the influence of the boundary on PDE-based covariance operators, Inverse Probl. Imaging 12 (5) (2018) 1083–1102.
- [35] U. Khristenko, L. Scarabosio, P. Swierczynski, E. Ullmann, B. Wohlmuth, Analysis of boundary effects on PDE-based sampling of Whittle-Matérn random fields, SIAM/ASA J. Uncertain. Quantif. 7 (3) (2019) 948–974.
- [36] G.-A. Fuglstad, F. Lindgren, D. Simpson, H. Rue, Exploring a new class of nonstationary spatial Gaussian random fields with varying local anisotropy, Statist. Sinica 25 (1) (2015) 115–133.
- [37] David Bolin, Kristin Kirchner, The rational SPDE approach for Gaussian random fields with general smoothness, J. Comput. Graph. Statist. 29 (2) (2020) 274–285.
- [38] David Bolin, Jonas Wallin, Multivariate type G Matérn stochastic partial differential equation random fields, J. R. Stat. Soc. B 82 (1) (2020) 215–239.
- [39] Edmond Chow, Yousef Saad, Preconditioned krylov subspace methods for sampling multivariate Gaussian distributions, SIAM J. Sci. Comput. 36 (2) (2014) A588–A608.
- [40] C. Soize, Non-Gaussian positive-definite matrix-valued random fields for elliptic stochastic partial differential operators, Comput. Methods Appl. Mech. Engrg. 195 (1) (2006) 26–64.
- [41] Patrick Moran, Statistical inference with bivariate gamma distributions, BiometrikaTrust 56 (1969) 627-634.
- [42] Johann Guilleminot, Christian Soize, Stochastic modeling of anisotropy in multiscale analysis of heterogeneous materials: A comprehensive overview on random matrix approaches, Mech. Mater. 44 (2012) 35–46.
- [43] J. Guilleminot, C. Soize, Stochastic model and generator for random fields with symmetry properties: Application to the mesoscopic modeling of elastic random media, Multiscale Model. Simul. 11 (3) (2013) 840–870.
- [44] C.N. Kelly, A.T. Miller, S.J. Hollister, R.E. Guldberg, K. Gall, Design and structure-function characterization of 3D printed synthetic porous biomaterials for tissue engineering, in: Advanced Healthcare Materials, Vol. 7, 2018, e1701095.
- [45] S. Adams, T. Dekker, J. Steele, K. Hamid, The use of patient-specific 3D printed titanium implants for complex foot and ankle limb salvage, deformity correction, and arthrodesis procedures, Foot Ankle Orthop. 2 (2017) 2473011417S0000.
- [46] Laura M. Ricles, James C. Coburn, Matthew Di Prima, Steven S. Oh, Regulating 3D-printed medical products, Sci. Transl. Med. 10 (461) (2018).
- [47] Yang Gao, Wan shen Xiao, Haiping Zhu, Snap-buckling of functionally graded multilayer graphene platelet-reinforced composite curved nanobeams with geometrical imperfections, Eur. J. Mech. A Solids 82 (2020) 103993.
- [48] Vu Thanh Long, Hoang Van Tung, Thermal postbuckling behavior of CNT-reinforced composite sandwich plate models resting on elastic foundations with tangentially restrained edges and temperature-dependent properties, J. Thermoplast. Compos. Mater. 33 (10) (2020) 1396–1428.